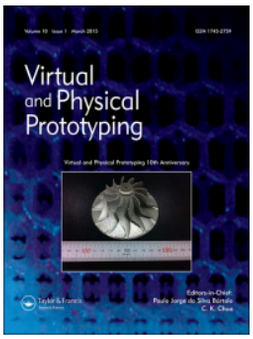

Virtual and Physical Prototyping

ISSN: (Print) (Online) Journal homepage: www.tandfonline.com/journals/nvpp20

3D-printing of architected calcium silicate binders with enhanced and in-situ carbonation

Nadia Ralston, Shashank Gupta & Reza Moini

To cite this article: Nadia Ralston, Shashank Gupta & Reza Moini (2024) 3D-printing of architected calcium silicate binders with enhanced and in-situ carbonation, Virtual and Physical Prototyping, 19:1, e2350768, DOI: 10.1080/17452759.2024.2350768

To link to this article: https://doi.org/10.1080/17452759.2024.2350768

Published online: 15 May 2024.

VIRTUAL AND PHYSICAL PROTOTYPING
2024, VOL. 19, NO. 1, e2350768 (15 pages)
https://doi.org/10.1080/17452759.2024.2350768

Taylor & Francis
Taylor & Francis Group

3D-printing of architected calcium silicate binders with enhanced and in-situ carbonation

Nadia Ralston, Shashank Gupta and Reza Moini

Department of Civil and Environmental Engineering, Princeton University, Princeton, NJ, USA

ABSTRACT

This paper investigates the use of architected cellular and solid designs of materials via additive manufacturing and in-situ CO_2 circulation to augment the carbonation and mechanical properties of a calcium silicate-based cement (CSC) binder. A wollastonite-based binder was formulated for extrusion-based 3D-printing. Solid and cellular lamellar architectures were designed to probe the role of layered interfaces and higher surface area on the degree of carbonation (DOC), respectively. Two carbonation exposure scenarios, with and without in-situ carbonation were employed. The DOC, microstructural phases, and flexural strength were characterised using TGA, modified over-flow image analysis technique, and three-point-bending, respectively. By exploiting 3D-printing and harnessing the higher surface area of cellular architecture, the material obtained a significantly higher DOC (by 8.9-folds) and flexural strength (by 5.7-folds) compared to reference cast. In-situ carbonation of cellular architected materials can additionally improve early-stage deformation, DOC (by 12.9-folds) and flexural strength (by 16.5-folds), compared to cast.

ARTICLE HISTORY
Received 9 February 2024
Accepted 28 April 2024

KEYWORDS
Architected materials; in-situ carbonation; cellular designs; 3D-printing; calcium silicate-based cement (CSC) binder

Highlights

- 3D-printing alone can enhance the uniformity of carbonation
- Cellular architecture and in-line carbonation increase DOC and strength
- In-line carbonation enhances both carbonation and buildability
- 3D-printing cellular wollastonite can lead to uniformity and enhancement of carbonation

1. Introduction

There has been a growing interest in additive manufacturing with construction materials to enable automated advancements in the structural design of cementitious materials [1–5]. Numerous opportunities remain to advance the 3D-printing processes, exploit design parameters, and take advantage of the flexibility of the manufacturing process in favour of the material's mechanical properties [6] and functional characteristics. For instance, the process and products can be advanced by the purposeful design of material arrangement or by the addition of in-situ features to tailor the interaction of the 3D-printed materials with their environment [7]. As the additive manufacturing of civil infrastructure materials and structures continues to grow, these opportunities [7] can be applied to a variety of hydraulic or non-hydraulic construction materials [8–12].

Calcium silicate-based cement (CSC) is a non-hydraulic material that relies on carbonation in which the material sequesters CO_2 from the atmosphere to solidify and harden [13]. The hardened calcium silicate-based cement (CSC) is produced partly from the same raw materials as ordinary Portland cement (OPC), forming reaction products including calcium carbonate and Ca-modified silica gel [13]. The low-lime CSC binders include wollastonite/pseudo-wollastonite ($CaO{\cdot}SiO_2$, in short CS) and rankinite ($3CaO{\cdot}2SiO_2$, in short C3S2) [13]. Since non-hydraulic reactivity increases with the decline of the Ca/Si ratio, wollastonite is known to outperform other non-hydraulic CSC binders [14].

Currently, there is no prior work in the literature that explores additive manufacturing of any type of low-lime binders (e.g. wollastonite, Pseudo-wollastonite, rankinite) to promote carbonation and overcome the carbonation limitations in the conventionally cast monolithic counterparts. Similarly, the flexibility to design and fabricate architected materials with purposeful arrangements to

CONTACT Reza Moini mmoini@princeton.edu Department of Civil and Environmental Engineering, Princeton University, 59 Olden St., Princeton, NJ, 08544, USA

enhance mechanical properties has remained underutilised for these types of non-hydraulic binders [15]. Through first formulating a CS binder for 3D-printing, here, we propose the design of these materials at small (mm) scale with a high surface area to volume ratio for which cellular architectures are a great contender. In addition to without in-situ carbonation printing where the deposited material is exposed to atmospheric carbonation, we examine the use of an in-situ CO_2 circulation during the 3D-printing process to *additionally* take advantage of the discretized 'filament-by-filament' characteristics of layered materials during the additive fabrication process in favour of CO_2 uptake and strength development. Although some have studied the application of pressurised CO_2 while printing OPC [7], there is no prior work that has explored an in-situ carbonation process with low-lime binders. Thus, two carbonation scenarios are employed during the printing process, which will henceforth be referred to as the 'without in-situ carbonation' (e.g. atmospheric carbonation during the printing) and 'in-situ carbonation' (i.e. in-situ carbonation using CO_2 circulation during the printing process). Both scenarios were followed by the same post-printing carbonation in a chamber.

The objectives of this study on wollastonite-based ($CaSiO_3$) binder are to (i) establish a suitable formulation for 3D-printing and design of cellular architected materials, (ii) understand the role of the material's cellularity in augmenting carbonation and strength development, and (iii) investigate the potential of in-line CO_2 circulation on the further enhancement of carbonation and strength (Figure 1).

2. Materials and methods

2.1. Material characterisation

The wollastonite powder (Vansil W-30) used was sourced from Vanderbilt Minerals. The X-ray diffraction (XRD) pattern of the powder was recorded using a Rigaku Miniflex X-ray Diffractometer operated at 50 kV and 30 mA. The diffraction pattern was obtained for the range of 2θ angles from 10° to 80° using a 0.4 deg/minute step. The XRD pattern (Figure 2) correlates well with the data for wollastonite/pseudo-wollastonite previously reported in the literature [16], where wollastonite/pseudo-wollastonite can be identified as the primary ingredient. The average particle size (D50) of the Vansil W-30 was reported as 7.5 microns as shown in Figure 3 [16,17].

2.2. Sample preparation

2.2.1. Materials formulation

Unlike OPC systems, the lack of a solidification mechanism in CSC binders, aside from carbonation, poses an additional challenge in obtaining early strength and buildability in the 3D-printing process [18–20]. Therefore, tuning the rheological properties of the binder, including adequate yield stress, is necessary to achieve 'printability' as characterised by sufficient buildability for these types of colloidal inks [21–23]. To tune the shear yield stress and enhance the early-age green strength, a low water-to-cement ratio compared to those typically used in cast formulations was explored along with inorganic (nanoclays) and organic (polymer) admixtures [24,25]. Nanoclays (NCs) have been reported to accelerate structural build-up kinetics and enhance the thixotropy [26–30], thus offering particular advantages in 3D-printing with colloidal materials. However, 3D-printing can lead to phase separation and bleeding phenomena under pressurised extrusion processes. Therefore, viscosity modifying admixtures (VMAs) are common in formulating colloidal suspensions as a means to obtain homogeneity in the binder under extrusion and to stabilise the consistency of the extrudate and

Figure 1. Three main approaches to enhance the carbonation and strength of CSC binders include (a) design of materials architecture, (b) additive manufacturing, and (c) two carbonation scenarios of without and with the in-situ carbonation using in-line CO_2 circulation nozzle, both followed by post-printing carbonation in a CO_2 chamber.

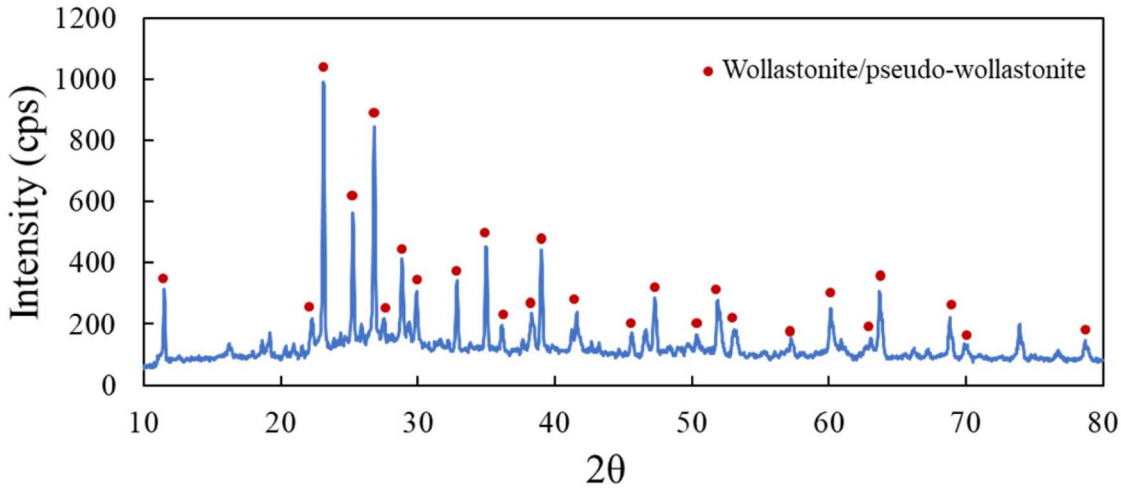

Figure 2. XRD pattern of uncarbonated wollastonite powder.

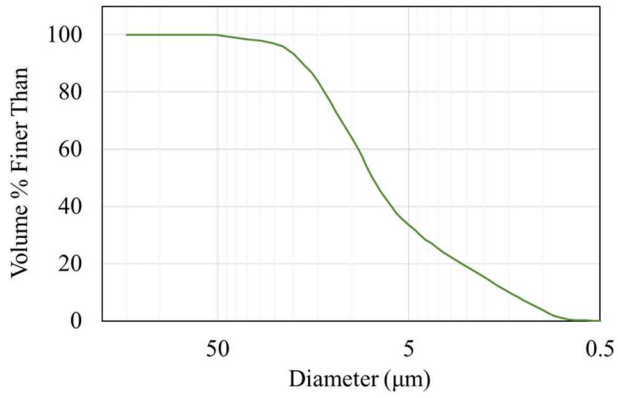

Figure 3. Particle size distribution of wollastonite powder.

flow [11]. Low molecular weight methylcellulose (MC) polymer is a type of VMA used in this study that can improve filament cohesion [31,32]. As a result, the formulated material in this study used a (w/c) of 0.5, 0.6% MC dosage by weight of cement (Table 1), and 3% NC dosage by weight of cement. The water-to-cement ratio selected is relatively higher than those used in hydraulic cement binder (w/c of 0.275) [24], which can be partly due to the smaller particle size and higher specific surface area of CSC binders compared to OPC [33,34].

2.2.2. Mixing procedure

Upon weighing the material, the dry MC was added to the powder. The deionised (DI) water with the added NC was poured over the dry powder containing MC and mixed in two steps using a Twister Evolution Venturi vacuum mixer to remove any large air bubbles. During the first 25 s of mixing, the binder was subjected to an initial pre-mixing mode with a 70% vacuum level followed by a 90-second mixing at 400 rpm. The binder was then mixed a second time for 90 s at 400 rpm and a 100% vacuum level. After mixing, the binder was loaded into the syringe and then fitted onto the extruder of the 3D-printer.

Table 1. Material formulation.

Wollastonite cement (g)	Water (g)	MC (g)	NC (g)
200 grams	100 grams	1.2 grams	6 grams

2.2.3. Design of material architecture

To examine the role of 3D-printing on the carbonation of wollastonite-based binder compared to its cast counterpart, two sets of sample designs were cast and 3D-printed: prismatic and single filaments. To specifically examine the role of the additive manufacturing process on carbonation uniformity, individual filaments with a nominal width of 2.95 mm and height of 1 mm were cast and 3D-printed.

Among the prismatic filaments, two architected prismatic designs were considered to examine the role of 3D-printing and the material's degree of cellularity on the carbonation and mechanical properties, as follows: (i) Solid lamellar (100% infill) and cellular lamellar (nominal 60% infill, corresponding to 73.4% solid) as demonstrated in Figure 4(a and b). All 3D-printed architected (Figure 4(a and b)) and cast (Figure 4(c)) prismatic samples were designed to have a width of 25 mm, height of 25 mm, and length of 80 mm.

2.2.4. 3D-printing and in-line CO_2 circulation

To develop a 3D-printer suitable for extruding CSC binder, a gantry-based system (Ultimaker 2 Extended + used for printing thermoplastic materials) and a stepper motor-driven extrusion system (Structur3d

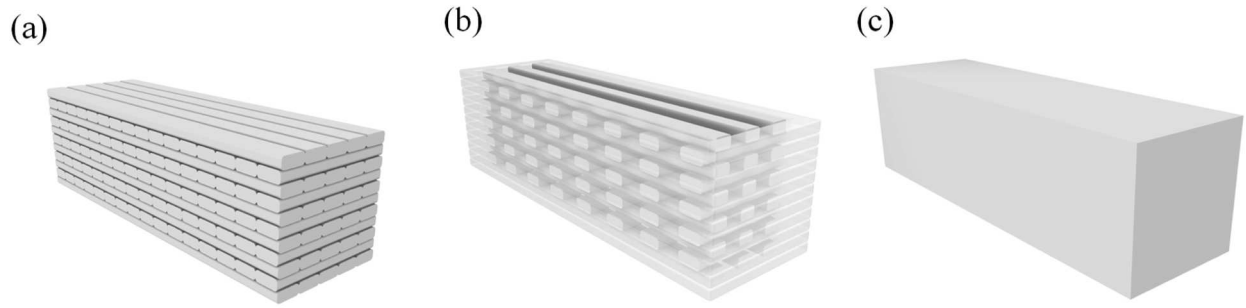

Figure 4. Schematic design of the (a) lamellar solid architected material with 100% infill (solid lamellar), (b) cellular architected material with 60% nominal infill (cellular lamellar), and (c) cast sample.

Discov3ry Paste Extruder) were merged (Figure 5(a)) [35–37]. For continuous binder delivery from the syringe to the nozzle holder assembly on the printer, a polyethylene tube with an internal diameter of 6.35 mm was connected from the selected nozzle to the syringe. Two nozzle designs were customised for extrusion with and without in-situ carbonation. A regular 'binder nozzle' (Figure 5(b)) was used for the without in-situ extrusion process. As part of the in-situ carbonation method (Figure 5(c, d, e)), a 'four-prong CO_2 nozzle' was designed that consists of four equidistant nozzles located in each orthogonal direction with an aperture in the centre for the extrusion of the CS binder. This allowed for in-line diffusion of CO_2 gas can reach the deposited material irrespective of the 3D-printing direction (Figure 5(e)). A polyethylene tube with an internal diameter of 9.23 mm is connected from the Airgas CO_2 cylinder to the 3D-printed inlet of the CO_2 nozzle as shown in Figure 5(c, d). The CO_2 nozzle was used to initiate the carbonation process immediately upon material extrusion, thus allowing for early carbonation of the filaments and interfaces during the print. The in-line printing was conducted under a fumed hood with constant monitoring of CO_2 concentration at the face and over the top of the printer due to safety limits. The temperature at the fume hood was in equilibrium with the temperature in the rest of the laboratory where other experiments were being conducted. During printing, the CO_2

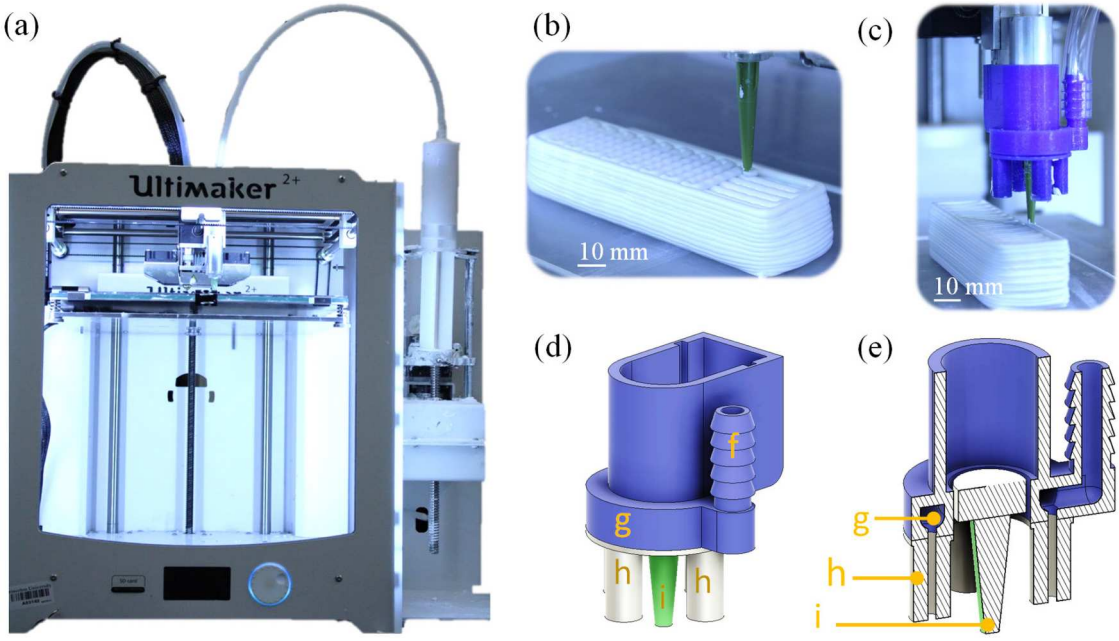

Figure 5. (a) Extrusion-based 3D-printer setup with (b) a regular binder nozzle or (c) a four-prong CO_2 nozzle attachment for in-situ carbonation, (d) a schematic 3D view of the CO_2 nozzle attachment that is friction-fitted into a custom-made aluminum nozzle holder, and (e) schematic cross-section view of the CO_2 nozzle attachment further detailed as follow: (f) polyethylene tube delivers CO_2 to the inlet, after which (g) an internal distribution cavity carries the air to (h) four different output nozzles (each 15 mm long), spaced evenly around the (i) CS binder nozzle (28.4 mm long). The offset between the tip of the nozzle (i) and the CO_2 output nozzles (h) is 13.4 mm.

concentration was measured to be between 1200 and 2400 ppm carbon dioxide at the face and over the top of the printer (within 18″) and between 600 and 1000 ppm at 5′ away from the printer (in the lab), for a source pressure ranging from 5 and 10 psi for each run. These values are signifncatly higher than the typical atmospheric CO_2 concentration in the lab. The samples were immediately moved to carbonation chamber upon completion of the fabrication.

Design of architected materials into a toolpath were enabled using a commercial slicer (Simplify3D). In this work, a printing speed of 750 mm/min, layer height of 1 mm, nominal filament width of 2.5 mm, extrusion multiplier of 3, and a 10% overlap between the perimeter and infill pattern were used.

2.2.5. Carbonation process

The solid and cellular lamellar 3D-printed prismatic samples were carbonated under the two scenarios, utilising 'without in-situ carbonation' and 'in-situ carbonation'. In the first, the material is exposed to atmospheric carbonation during printing, and in the latter, the sample is exposed to in-situ carbonation. Both processes are followed by the carbonation of the material in a controlled chamber environment (Figure 6) upon fabrication. The carbonation chamber's conditions were set to a temperature of 37°C, 95% relative humidity (RH), and 20% CO_2 concentration for all samples. These conditions were selected based on the experimentally determined parameters previously reported for the maximum amount of $CaCO_3$ during carbonation of 50–72 hours for low-lime calcium silicates [16]. The Airgas CO_2 (40 High-Pressure Steel Cylinder) was used as a source and was connected to the carbonation chamber. Once in the chamber, the casts and 3D-printed samples were exposed to carbonation for 72 hours. The 3D-printed samples were cured on a PMMA (Poly-methyl methacrylate) substrate sheet and exposed otherwise, while cast samples were cured on the PMMA substrate in a thin PLA mold with exposed top surface.

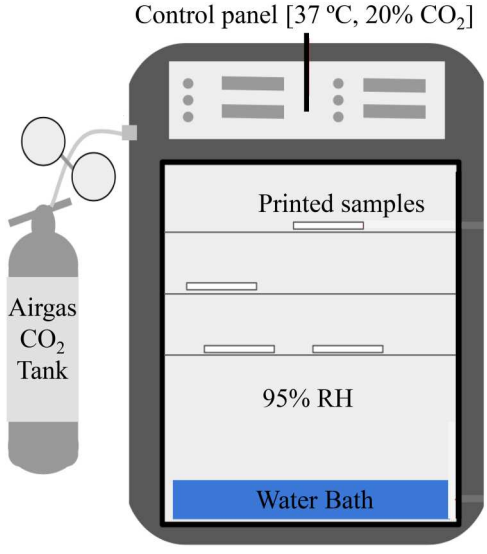

Figure 6. Illustration of the carbonation chamber setup and settings.

2.3. Microstructural characterization

Immediately after a sample was removed from the carbonation chamber, the samples were wrapped in a plastic film and kept in a vacuum until testing. The samples were tested within 48 hours after being removed from the chamber. The degree of carbonation (DOC) was investigated using a scanning electron microscope (SEM) and image analysis, thermogravimetric analysis (TGA), and phenolphthalein indicator on both the prismatic 3D-printed and cast materials as well as the single filament 3D-printed and cast materials.

2.3.1. Thermogravimetric analysis (TGA)

For analyzing the small cast and 3D-printed single filaments, specimen taken from the exterior and interior of the entire carbonated cast and 3D-print materials were grounded. For analyzing the large prismatic materials, a representative powder was carefully collected from the centre of the samples to assess the carbonation depth through the material. In preparation for the TGA analysis, the carbonated specimens were ground using a mortar and pestle and approximately 30 mg of the powder was placed in the Perkin Elmer TGA-8000 GC/MS chamber that was purged with nitrogen (N_2) gas. The characterisation was programmed to maintain isothermal conditions of 23°C for the first 10 min, followed by heating to 1000°C at a constant rate of 10°C/min. This temperature ramp was considered given that the 500–900°C range is where the weight loss of the material due to the decomposition of calcium carbonate ($CaCO_3$) and the subsequent release of CO_2 takes place [13,38,39]. The tangent method is often employed in TGA analysis to exclude the influence of C–S-H decomposition. However, the range of $CaCO_3$ decomposition (500–900 °C) is significantly higher than where we would expect for the decomposition of C–S-H (300 °C), if any [40]. Additionally, the decomposition of calcium carbonate often exhibits multiple inflection points due to the various polymorphs that can decompose at various temperatures within the 500–900 °C range. For these two reasons, the tangent method is not suitable for correcting the decomposition of $CaCO_3$ due to the decomposition of

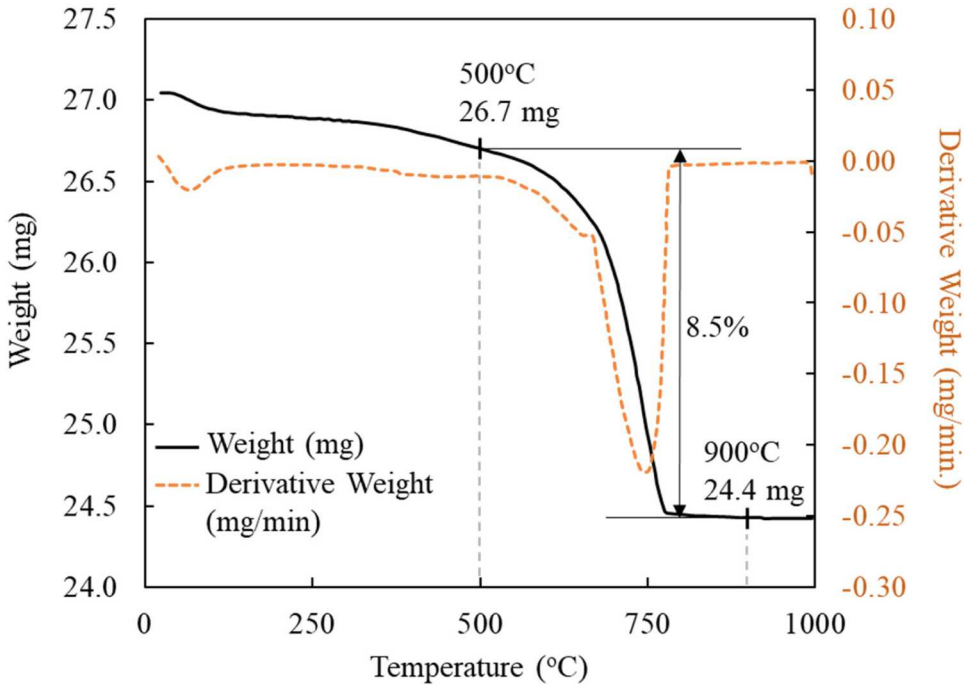

Figure 7. Representative dissociation of carbonated wollastonite during a TGA test demonstrating weight loss for a sample extracted from a single filament.

other products. The direct weight loss (wt.%) of $CaCO_3$ was calculated using the inflection points of the differential thermogravimetric (DTG) curves that marked this decomposition range [38], as shown in Figure 7. For similar experimental conditions as the one used in this study (considering temperature, CO_2 concentration, exposure duration, and disregarding the difference in particle size distribution), researchers have reported that the carbonation of wollastonite can form up to 43.71% of $CaCO_3$ by mass [16]. This value was used in determining the degree of carbonation for the single filament and cast samples in Equation 1 based on the calculated amount of $CaCO_3$(%) decomposed in the carbonation of each specimen.

$$\text{Degree of carbonation (DOC)} = \frac{\text{Amount of } CaCO_3 \text{ (wt\%) at time, } t}{\text{Maximum amount of } CaCO_3\text{(wt\%)}} \text{ for the specific binder \& conditions}, \quad (1)$$

2.3.2. Scanning electron microscopy (SEM) characterization

The microstructure of the 3D-printed and cast single filaments was investigated using the backscattered electron (BSE) mode of the Verios 460 XHR scanning electron microscope. The specimens were first cured in the carbonation chamber for 72 hours and submerged in isopropyl alcohol for 24 hours [41]. They were then transferred into the low-viscosity epoxy (Spurr™) in cylindrical molds and placed in vacuum (−1 bar) at room temperature for 24 hours. Subsequently, the molds were cured in an oven for 48 hours at 65 °C for an epoxy hardening [42]. The specimens were then obtained from the mold and cut using the diamond saw, lubricated with isopropyl alcohol, to obtain the cross-sectional surface of the filaments. Using the Allied Multi-prep polisher, the cross-sectional surface of the specimen was sequentially polished with silicon carbide abrasive papers of 120, 240, 320, 400, and 600 grits and then with diamond pastes of 6, 3, 1, and 0.25 μ*m*. Each specimen was polished for 8 minutes with a rotation of 90° after 1 min to eliminate the radial scratches [43]. The specimens were then sputter-coated with a 15 nm-thick layer of Iridium using the Leica EM ACE600 sputter coater. Finally, the specimens were electrically grounded by connecting the conductive Iridium layer on top of the specimen with the SEM sample holder using copper strips. The SEM was operated in high vacuum mode with an accelerating voltage of 20 keV and a working distance of 10.00 mm.

2.3.3. Image analysis

A robust modified-overflow method was used to determine the threshold value based on the Fourier-fit function (or any other fitting functions) of the segmented area vs. grayscale intensity value plot, and its

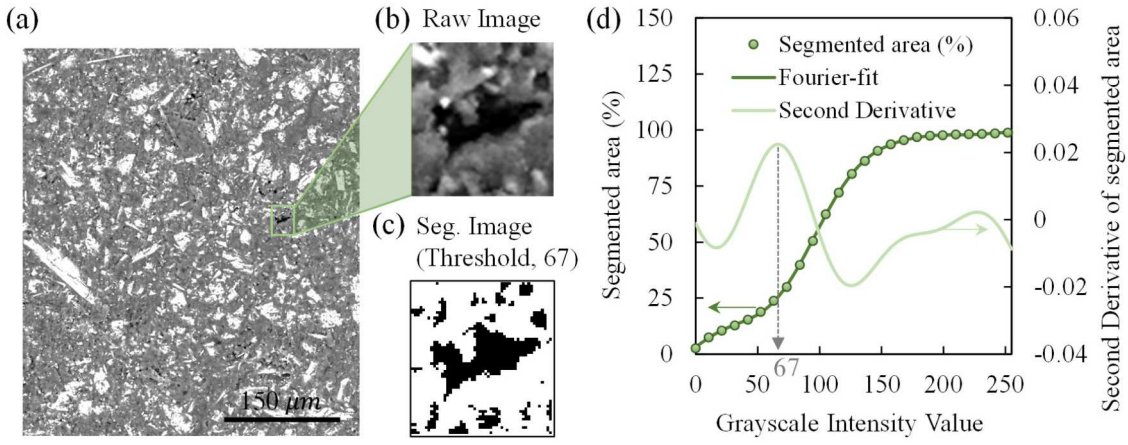

Figure 8. (a) BSE-SEM image of hardened wollastonite-based binder, (b) a small section containing the pore phase and the corresponding (c) segmented section using threshold value obtained from the modified overflow method shown in (d) the plot of the segmented area (%) vs. the grayscale intensity values using a Fourier-fit and the corresponding local maxima of the second derivative.

corresponding first and second derivatives. A modified-overflow method is used for image analysis as presented in Figure 8, where, similar to a conventional overflow method [44], a small section containing pores (Figure 8 (b)) was first selected from the BSE image of hardened microstructure (Figure 8(a)). The segmented area (Figure 8(c)) as the function of the grayscale intensity value was then plotted as shown in Figure 8(d). Subsequently, the Fourier series function was employed for the curve fitting [45] of the area vs. grayscale intensity plot (Figure 8(d)). This is followed by plotting the corresponding second derivative of the Fourier-fit (Figure 8(d)) instead of using a tangent-slope method [44]. This is to avoid limitations of the grayscale intensity values and to allow for better determination of the threshold value directly. The local maxima of the second derivative between the two constant slope regions of the Fourier-fit function corresponded to the threshold value of 67, as presented in the segmented image of Figure 8(c), using the raw image shown in Figure 8(b). A similar approach was employed to calculate the threshold value for unreacted wollastonite by selecting the section containing this phase from the BSE image and applying the same steps described for Figure 8(c). Overall, 15 sections were considered to calculate the average lower and upper grayscale intensity threshold values corresponding to pores and unreacted wollastonite. The proposed modified-overflow thresholding method was used for the ternary segmentation of the BSE images to quantitively determine the percentage distribution of the different microstructural phases, using in-house developed MATLAB® 2022a code [46].

2.4. Mechanical properties characterization

The material's flexural strength was characterised using a three-point bending (3PB) test for solid and cellular 3D-printed and cast samples. The hardened prismatic samples (with average dimensions of 25 mm x 25 mm x 80 mm) were designed per ASTM C78/C78 M specifications [47] as illustrated in Figure 9. The loading rate was set to 0.01 mm/min. After carbonation and preparation of the samples for testing, the dimensions and mass were measured, and the bulk density was calculated. The voids (porosity) of the cellular sample was not considered in the calculation of the overall MOR as they are treated as monolithic similar to cast and solid 3D-printed cases in plotting the MOR values. The specific MOR would demonstrate further enhancement if the architected porosity is considered.

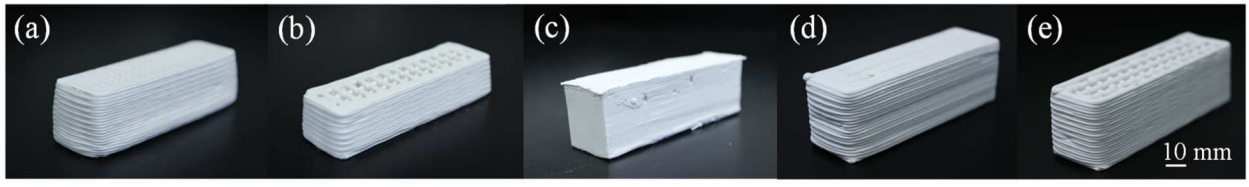

Figure 9. (a,b) The solid and cellular lamellar architecture 3D-printed without in-situ carbonation, (c) the reference cast, and (d,e) the solid and cellular lamellar architecture 3D-printed in the presence of the in-situ carbonated nozzle.

3. Results

3.1. Thermogravimetric analysis

3.1.1. Carbonation of single-filaments

The analysis for the degree of carbonation for the single filament samples was conducted for the exterior and interior of the cast and 3D-printed filaments to capture insight into the carbonation phenomena at the surface vs. the core of the material as illustrated in Figure 10(a and b). The analysis demonstrates no significant difference (using f-test and t-test, with a 95% confidence interval) in the degree of carbonation at the exterior of the cast and 3D-printed sample (Figure 10(c)). In other words, the single filament cast, and single filament 3D-printed samples exhibit similar carbon uptake at the exterior surfaces. However, when the interior of both samples is examined, a statistically significant difference between the degrees of carbonation is identified (using f-test and t-test, with a 95% confidence interval). Both the cast and 3D-printed materials exhibit relatively consistent DOC, and, thereby, relatively uniform carbonation between the interior and exterior.

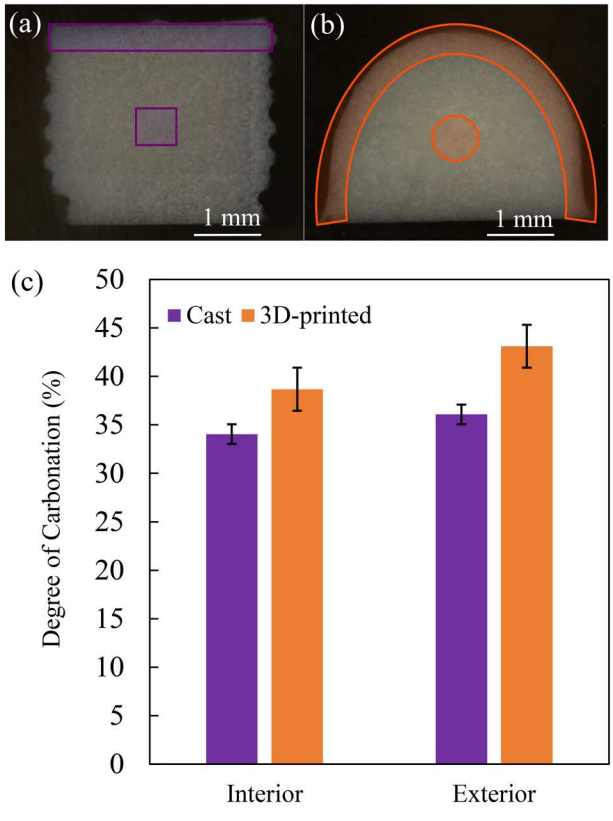

Figure 10. Thermogravimetric analysis (TGA) of the exterior vs. the interior of the (a) cast vs. (b) 3D-print materials for the (c) comparison of the degrees of carbonation.

3.1.2. Carbonation of prismatic architected materials

The degree of carbonation of the prismatic architected 3D-printed samples was analyzed by comparing the material from the core of each sample (solid lamellar and cellular lamellar) to that of the reference cast (Figure 11(a)). In the process of without in-situ carbonation 3D-printing and post-carbonation, the solid lamellar architected material significantly outperformed the cast counterparts. The samples with in-situ carbonation (Figure 9(d, e)) demonstrated slightly higher layer height and sample height that can be hypothesised due to the early-stage carbonation, in comparison to the samples without in-situ carbonation (Figure 9(a, b)).

The cellular architected materials exhibit a statistically significant increase in the degree of carbonation compared to the solid lamellar counterparts, leading to a significant increase in DOC from cast to cellular lamellar architected materials. It is noted that the difference in DOC is greater between the cellular and solid lamellar prismatic cases than between the cast and the solid lamellar cases. This finding suggests that while the use of 3D-printing can improve carbonation, the degree of cellularity in the design is important in facilitating further carbonation in wollastonite-based binders.

The degree of carbonation of architected 3D-printed samples fabricated using the in-line CO_2 nozzle for the in-situ carbonation process was analyzed using the materials at the core of each sample (solid lamellar and cellular lamellar) and compared to that of the conventionally 3D-printed counterparts (without in-line CO_2 nozzle) as illustrated in Figure 11(b). Using the in-situ carbonation process, an additional statistically significant increase in DOC was found when comparing both solid and cellular lamellar architected materials fabricated using the in-line CO_2 during the print with their counterparts without in-line CO_2 (Figure 11(b)).

The results highlight two new insights about carbonation using the in-situ process. First, in the presence of in-situ carbonation during 3D-printing, the cellular-architected materials significantly outperform the solid counterparts in terms of the degree of carbonation. Second, there is a notable increase in carbonation due to the in-situ carbonation process in the solid and cellular architected materials compared to their cast counterparts. The cellular lamellar architected materials that underwent in-situ carbonation significantly outperformed the cellular counterparts that were carbonated only using the without in-situ carbonation 3D-printing

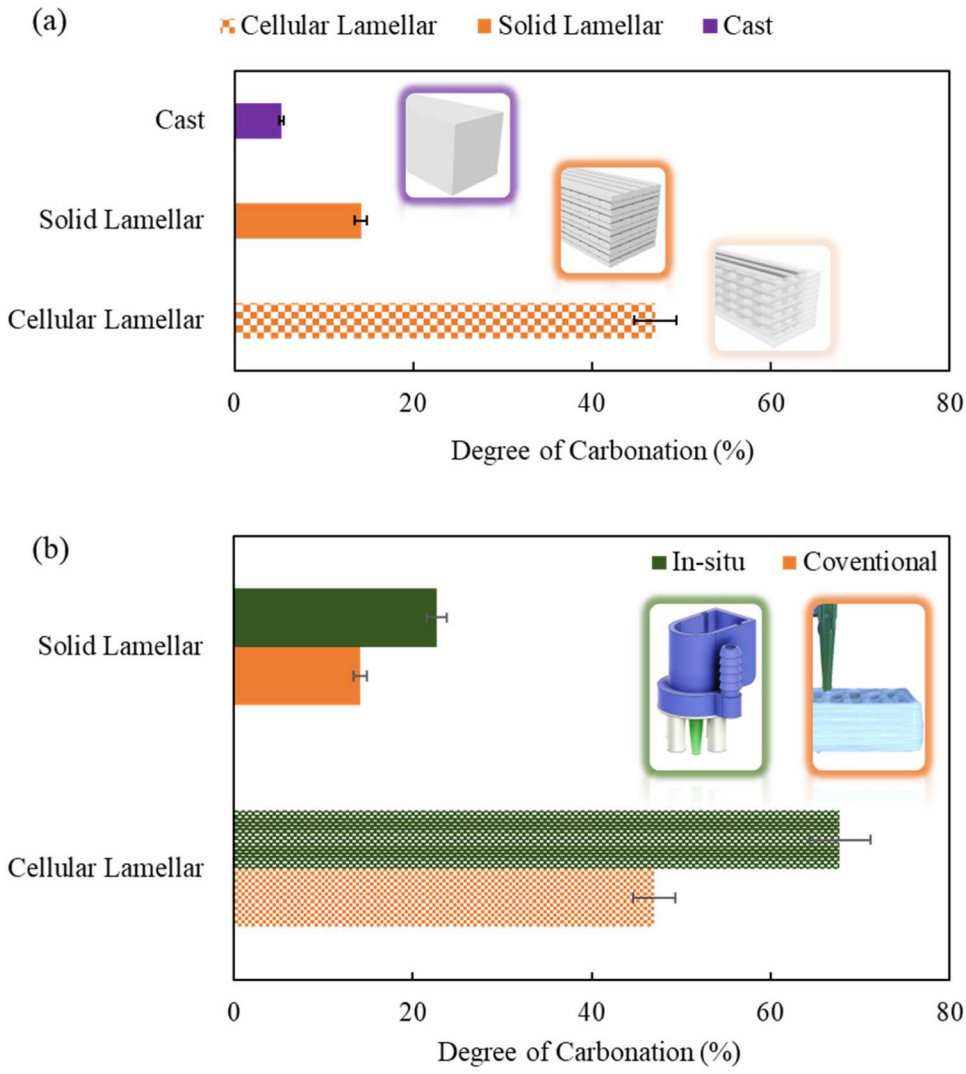

Figure 11. Comparison of the degrees of carbonation for (a) each without in-situ carbonation (conventional) prismatic design and (b) comparison of the degrees of carbonation between the two without in-situ and in-situ-carbonation processes.

process by approximately 44%. Similarly, solid lamellar architected materials that underwent in-situ carbonation significantly outperformed the solid counterparts that were carbonated only using the without in-situ carbonation 3D-printing process by 60%. This suggests that in-situ carbonation can provide further enhancements over those obtained merely from 3D-printing. These enhancements lead to improvements of DOC over the cast counterparts with the normal post-carbonation process for the cellular and solid lamellar materials. This can be due to the compound effects of the in-line diffusion of higher concentrations of CO_2 and the higher surface area of cellular materials available for carbonation from the early stages of extrusion. The results provide supportive evidence for our hypothesis that cellularity and in-situ carbonation can enhance the carbonation process in CS binders.

3.2. Phase analysis of single-filaments

The spatial distribution of the microstructural phases in the hardened cast and 3D-printed wollastonite-based binder was investigated using the segmented BSE-SEM cross-sectional images with ternary phases on single 3D-printed filaments and cast specimens. The average volume percentage of three microstructural phases, namely pores, reacted products, and unreacted wollastonite, was calculated from the total volume taken at the top, centre, and bottom of the cast and 3D-printed filament (Figure 12(a, b)), as presented in Figure 12(c). The comparison of reacted product in 3D-printed filament vs. reference cast filament depicted in Figure 12(c) corresponds with the results seen in TGA analysis for the single filament samples (Figure 10(c)), in that the 3D-printed filament exhibits an overall higher degree of carbonation than the cast counterpart.

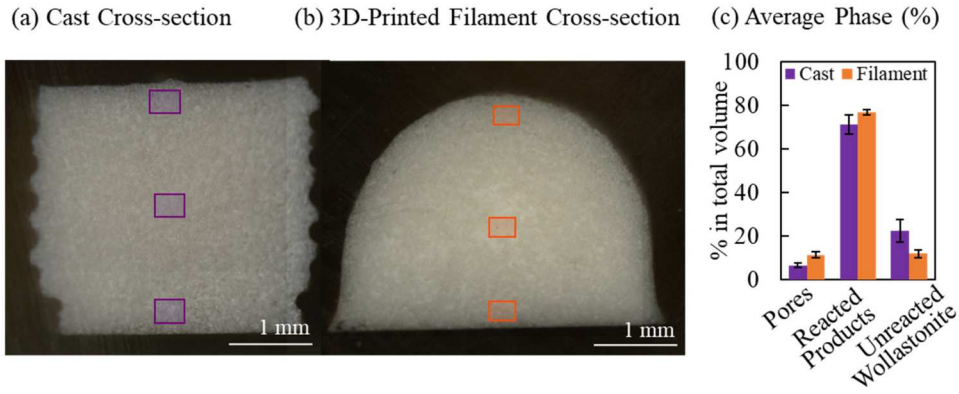

Figure 12. (a) Cross-section of the cast filament and (b) 3D-printed single filament, and (c) the average percentage of three microstructural phases in the total volume of either sample type.

3.3. Flexural strength

To better understand the relationship between the degree of carbonation and flexural strength in cellular and solid architected materials in comparison to reference cast counterparts, the average modulus of rupture (MOR) was probed and characterised for both conventionally carbonated (without in-line CO_2 nozzle) and in-situ carbonated materials (Figure 13). The conventionally 3D-printed solid lamellar architecture demonstrated a statistically significant increase in flexural strength compared to the cast material as seen in Figure 13(a) (using f-test and t-test, with a 95% confidence interval). Additionally, a significant increase in strength in cellular architected material was observed from the solid lamellar architected materials and the cast (Figure 13(a)).

The analysis of the flexural strength of architected materials that underwent the in-situ carbonation process during 3D-printing was conducted in comparison to conventionally 3D-printed materials as illustrated in Figure 13(b). The solid lamellar architected materials that have undergone the in-situ carbonation demonstrated a significant increase in flexural strength values

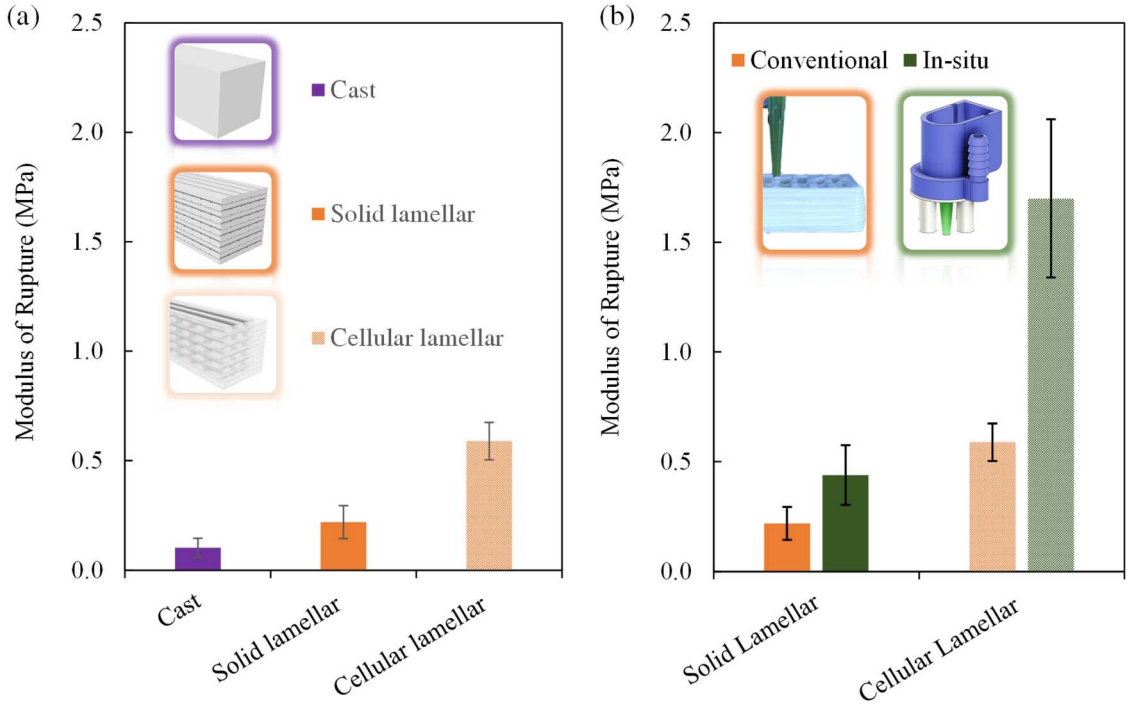

Figure 13. (a) Flexural strength characterised by MOR of carbonated architected materials fabricated using without in-situ carbonation (conventional) 3D-printing and carbonation process in comparison to cast counterparts, and (b) Comparison of MOR of architected materials fabricated using in-situ carbonation process during 3D-printing with the conventionally 3D-printed counterparts.

compared to conventionally 3D-printed material. Similarly, and more significantly, the cellular architected material that has undergone the in-situ carbonation process demonstrated a significantly higher strength.

The results represent a statistically significant enhancement of strength in both solid and cellular lamellar materials from the cast. Such an augmentation of strength is found more substantial in the cellular materials than in the solid counterparts, relative to the cast. In other words, the in-situ carbonated solid lamellar architected materials represent almost twice the flexural strength relative to that of the conventionally 3D-printed counterparts while the in-situ carbonated cellular lamellar designs exhibit almost triple the flexural strength of the conventionally 3D-printed counterparts. Probing DOC and strength indicates that carbonation and strength are both promoted by 3D-printing, cellular design, and in-situ carbonation process to various degrees with potentially synergistic effects.

4. Discussion

Using the in-situ carbonation with a gas diffusion nozzle in the cellular architected materials significantly enhanced the flexural strength compared to cellular designs that underwent only post-carbonation, leading to a higher flexural strength compared to cast counterparts. As curing continues, we can hypothesise that the 'filament-by-filament' discretized characteristics in the solid 3D-printed material and higher surface area in the cellular material promote greater CO_2 uptake and carbonation product. This hypothesis can explain the higher degree of carbonation that is measured at the centre of the 3D-printed solid and cellular materials compared to the centre of the cast counterparts (Figure 11(a)). Similarly, the lower MOR of the cast can be explained by the lower degree of carbonation of the cast compared to the 3D-printed solid and cellular lamellar.

It must be noted that the degree of carbonation can also depend on the sample size or thickness due to the time-dependent nature of carbonation. The increase in monolithic sample size between the single filament to prismatic designs from 2 mm (Figure 10) to ~ 25 mm (Figure 11(a)) led to significant drops in DOC for the cast and solid lamellar samples, respectively.

The cast samples at the size of a single filament (Figure 10) present significantly higher DOC compard to larger bulk samples (Figure 11(a)). In other words, as the size of the sample increases, the degree of carbonation in the cast decreases. It can be hypothesised that as the diffusion distance increases (with increasing sample size), the overall DOC decreases. This further alludes to the carbonation process as a function of depth which can be the subject of further investigations across cast and 3D-printed CS binders. Although researchers have assumed uniform carbonation in CSC binders tested under compression [48], such uniformity has not been well-studied and was not assumed in this work. The flexural strength was used to measure overall strength and, in principle, we hypothesise enhancement in compressive strength due to the relationship between flexural and compressive strength. However, non-uniform carbonation can intervene with this effect. In the presence of architected porosity, the absolute values of flexural or compressive properties may be enhanced, in the presence of higher DOC in the cellular vs the monolithic cast without architected porosity. Otherwise, the degradation of mechanical properties with increased porosity is indicated from a fundamental porosity-compressive strength relationship [49].

To examine the assumption of uniformity of carbonation, both the conventionally and in-situ carbonated 3D-printed architected material were examined against the cast material using a phenolphthalein indicator solution. The phenolphthalein indicator solution was applied to the cross-section of fractured samples from the three-point bending test samples that were carbonated and hardened for 3 days. The investigation elucidated the uniformity of carbonation and the role of the material's solid and cellular design on carbonation. The pH indicator is a 1% ethanol solution with 1 g of phenolphthalein and 90 mL 95.0 V/V% (volume per volume) ethanol diluted in water to 100 mL [50]. During carbonation, the diffused CO_2 hydrates to H_2CO_3 which then ionises to H^+, HCO_3^-, and CO_3^{2-} [51]. While uncarbonated wollastonite has a pH of 9.9–10, carbonation instantaneously drops the pH by approximately 3 units [31,34]. For this reason, when the phenolphthalein indicator solution is applied to the material, we would expect any carbonated regions to remain white and those uncarbonated to turn pink [52]. The phenolphthalein pH indicator was applied to the cross-section of each fractured sample from the 3PB test and then examined under a microscope to identify areas of carbonation (Figure 14).

It was found that the conventionally carbonated cellular specimens (Figure 14(a)) were uniformly carbonated as indicated by the white surface after applying the phenolphthalein pH solution. Some amounts of non-uniform carbonation were observed in the core of the conventionally carbonated lamellar sample as indicated by the faint pink colouring in the centre in Figure 14(b). In contrast, it is observed that the major centre region of the cast specimen (Figure 14(c)) yielded a pink colour upon contact with the pH indicator solution while a white region remains at the bottom,

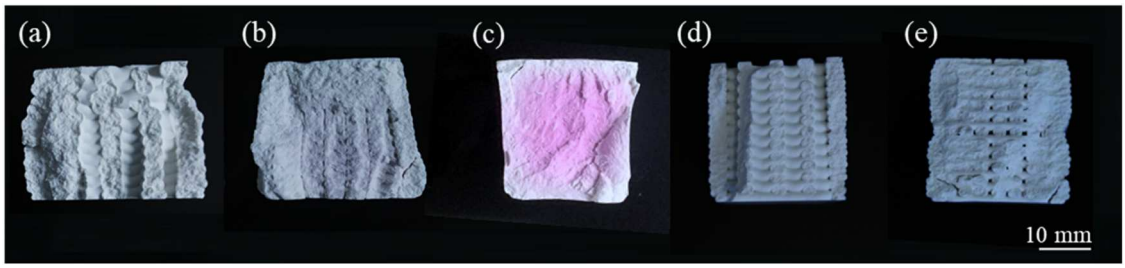

Figure 14. Cross-sectional areas of the without in-situ carbonation carbonated (a) cellular lamellar architecture, (b) solid lamellar architecture, and (c) cast samples, in comparison with the in-situ carbonated (d) cellular lamellar, and (e) solid lamellar immediately after exposure to the pH phenolphthalein solution.

top, and sides of the cross-section. Moreover, the in-situ carbonated cellular lamellar (Figure 14(d)) and solid lamellar specimens (Figure 14(e)) demonstrated uniform carbonation in their entire cross-section.

The results are indicative of non-uniform carbonation in the cast counterparts with significantly less carbonation occurring in the centre region in comparison to the nearly uniform carbonation in all 3D-printed architected materials. The non-uniformity in the 25 mm × 25 mm cross-section of the cast specimen can be reported as an average horizontal and vertical less carbonated core region of 19.81 and 21.24 mm. The carbonation depth analysis using the phenolphthalein experiment along with the conventionally and in-situ carbonated counterparts generally corroborates with the findings of the TGA analysis (Figure 11) and flexural strength (Figure 13) analyses in terms of the correlation between the higher overall degree of carbonation and enhanced mechanical properties across the three types of materials studied here (cast, solid, and cellular).

When comparing the solid lamellar samples with and without in-situ carbonation, particular attention was given to the first several layers of the prism. There is a notable reduction in early-age deformation in the solid lamellar architected samples fabricated using the in-situ carbonation method (Figure 9(a) vs. Figure 9(d), Figure 9(b) vs. Figure 9(e), Figure 14(a) vs. Figure 14(d), and Figure 14(b) vs. Figure 14(e)). The same observation was made in the fabrication of cellular architected by comparing samples processed with and without in-situ carbonation. As a result, both the solid and cellular lamellar architectures achieved enhanced shape stability, potentially induced by the in-situ carbonation leading to higher structural build-up rate and yield stress. The qualitative improvement of early-age deformation and corresponding rheological properties of the freshly 3D-printed CS-binder can be further studied to explore the potential of in-situ hardening of materials by carbonation to achieve taller structures, such as those explored in two-component robotic additive extrusion with concrete [24,25]. These observations suggested that the in-situ carbonation can expedite the early strength development and improve the early-age yield strength in carbonation-activated binders.

It must be noted that the highest absolute MOR value of the 3-day-old wollastonite-based binder obtained in this study (averaged at 1.70 MPa for cellular materials with 60% nominal porosity) is comparatively lower than the hydraulic OPC binder (averaged at 3.9–4.9 MPa) at the same age and similar w/c ratio [53–55]. Although the absolute flexural strength of the wollastonite-based binder is lower than that of OPC, even after enhancement of carbonation using in-situ carbonation of cellular designs, the strength can be analyzed considering the amount of material used. Considering the nominal 60% cellularity of the wollastonite-based binder compared to the monolithic OPC counterparts, the relative MOR increases to 4.25 MPa which compares similar to the 3.9–4.9 MP range reported for OPC of the same w/c and age [53–55]. Additional considerations regarding the associated emission of the materials used for these two types of cement can be considered in comparing the mechanical properties.

5. Conclusions

The design of construction materials has remained constrained to and limited by the monolithic casting of solid components. These restrictions have prohibited achieving more efficient materials and structures and overcoming often mutually exclusive material properties of engineered materials, such as strength and lightweight. Automation in fabrication of construction materials provides the ability to develop bespoke platforms that can accommodate bottlenecks in improving materials properties (e.g. carbonation, etc.). This work highlights an opportunity to utilise 3D-printing approach to utilising 3D-printing technology to augment the carbonation and mechanical properties of CSC binders by designing

cellular-architected materials and advancing the extrusion process.

The findings indicate that 3D-printing alone can provide a new pathway for carbonation by taking advantage of the discretized 'filament-by-filament' nature of the fabrication to address challenges of uniformly carbonating CSC binders that is otherwise limited by the casting of monolithic components. The results suggest that significant enhancement of the degree of carbonation can be made possible by facilitating higher surface area and consequently greater CO_2 uptake in the cellular network of 3D-printed material, compared to monolithic cast counterparts.

The in-situ carbonation of the cellular architected materials further demonstrates the ability to take advantage of the controlled nature of the 3D-printing process in favour of material properties. The results demonstrate that in-line CO_2 circulation can promote a greater diffusion of CO_2 throughout the cellular network of the materials interfaces, significantly enhancing the strength development compared to cast counterparts. This can be due to the compound effects of the in-line diffusion of higher concentrations of CO_2 and the higher surface area of cellular materials available for carbonation from the early stages of extrusion, which can be exploited using high surface/volume ratio designs of architected materials and customised printing processes. Enhanced strength-to-weight ratio can then be achieved using the in-situ carbonation of cellular designs of wollastonite-based binders, leading to similar mechanical properties compared to OPC.

In summary, the design of materials architecture, paired with advanced processing enabled by a specialised in-line CO_2 nozzle during the 3D-printing of materials can enable more efficient construction materials that rely on carbonation to gain strength. Besides, raw materials availability and carbon footprint, one of the main limitations of the proposed endeavours is the scalability of the in-situ carbonation process that would require retrofitting currently adopted carbonation curing equipment at large scale with additive manufacturing platforms for CO_2 delivery. Nevertheless, fabrication using in-situ carbonation may allow for facile on-site printing. In addition, 3D-printing cellular materials with intentional voids can be facilitated by the design and fabrication process, thus, higher geometric freedom in complex structures can be fulfilled while reducing materials usage [56]. The open porous structures created through this process can be further engineerd for heat transfer to allow for lightweight and energy-efficient structures [57]. Future research in understanding the role of water, carbonation depth, and the exposed surface-to-volume ratio can further inform design strategies for a wide range of non-hydraulic binders to solidify and obtain higher strength via carbonation.

Acknowledgment

The authors acknowledge the use of Princeton's Imaging and Analysis Center (IAC), National Science Foundation (NSF) Materials Research Science and Engineering Center (MRSEC; DMR-2011750) through Princeton Center for Complex Materials (PCCM). The authors would like to thank the National Science Foundation for their support (CMMI, No. 2129566). Special thanks are also given to Princeton University's Department of Civil and Environmental Engineering, School of Engineering and Applied Science (SEAS) Senior Thesis Funding, and Andlinger Center for all their financial support. The authors would like to thank Dr. Aimane Najmeddine and Mr. Arjun Prihar for their contributions to the image analysis method and TGA experiment, and Mr. Joseph Vocaturo for assisting with the installation of CO_2 cylinders and regulators.

Disclosure statement

No potential conflict of interest was reported by the author(s).

Funding

This work was partially supported by National Science Foundation: [Grant Number 2129566]; Princeton Center for Complex Materials: [Grant Number 2011750].

Contributions

Nadia Ralston: Conceptualization, Methodology, Investigation, Validation, Formal Analysis, Writing – Original Draft, Writing – Review & Editing, Visualization. Shashank Gupta: Visualization, Software, Formal Analysis, Writing – Review & Editing. Reza Moini: Conceptualization, Methodology, Investigation, Writing – Review & Editing, Funding acquisition.

Data availability statement

The data that support the findings of this study are available from the corresponding author, [RM], upon reasonable request.

ORCID

Shashank Gupta http://orcid.org/0000-0002-1192-9603
Reza Moini http://orcid.org/0000-0003-3117-6212

References

[1] Mechtcherine V, Nerella VN, Will F, et al. Large-scale digital concrete construction – CONPrint3D concept for

on-site, monolithic 3D-printing. Autom Constr. 2019;107:102933. doi:10.1016/j.autcon.2019.102933
[2] Ooms T, Vantyghem G, Van Coile R, et al. A parametric modelling strategy for the numerical simulation of 3D concrete printing with complex geometries. Addit Manuf. 2021;38:101743. doi:10.1016/j.addma.2020.101743
[3] Prihar A, Gupta S, Esmaeeli HS, et al. Tough bouligand and double-bouligand architected concrete enabled by two-component robotic additive manufacturing. SSRN Electron J. 2023. doi:10.2139/ssrn.4345483
[4] Prihar A, Garlock MEM, Najmeddine A, et al. Mechanical performance of sinusoidally architected concrete enabled by robotic additive manufacturing. Mater Des. 2024;238:112671. doi:10.1016/j.matdes.2024.112671
[5] Khan MS, Sanchez F, Zhou H. 3-D printing of concrete: beyond horizons. Cem Concr Res. 2020;133:106070. doi:10.1016/j.cemconres.2020.106070
[6] Buswell RA, Leal de Silva WR, Jones SZ, et al. 3D printing using concrete extrusion: a roadmap for research. Cem Concr Res. 2018;112:37–49. doi:10.1016/j.cemconres.2018.05.006
[7] Tay YWD, Lim SG, Phua SLB, et al. Exploring carbon sequestration potential through 3D concrete printing. Virtual Phys Prototyp. 2023;18:e2277347. doi:10.1080/17452759.2023.2277347
[8] McLellan BC, Williams RP, Lay J, et al. Costs and carbon emissions for geopolymer pastes in comparison to ordinary Portland cement. J Clean Prod. 2011;19:1080–1090. doi:10.1016/j.jclepro.2011.02.010
[9] Xia M, Sanjayan J. Method of formulating geopolymer for 3D printing for construction applications. Mater Des. 2016;110:382–390. doi:10.1016/j.matdes.2016.07.136
[10] Raza MH, Zhong RY, Khan M. Recent advances and productivity analysis of 3D printed geopolymers. Addit Manuf. 2022;52:102685. doi:10.1016/j.addma.2022.102685
[11] Douba A, Badjatya P, Kawashima S. Enhancing carbonation and strength of MgO cement through 3D printing. Constr Build Mater. 2022;328:126867. doi:10.1016/j.conbuildmat.2022.126867
[12] Farnam Y, Villani C, Washington T, et al. Performance of carbonated calcium silicate based cement pastes and mortars exposed to NaCl and MgCl2 deicing salt. Constr Build Mater. 2016;111:63–71. doi:10.1016/j.conbuildmat.2016.02.098
[13] Ashraf W, Olek J, Jain J. Microscopic features of non-hydraulic calcium silicate cement paste and mortar. Cem Concr Res. 2017;100:361–372. doi:10.1016/j.cemconres.2017.07.001
[14] Wang X, Guo M-Z, Ling T-C. Review on CO2 curing of non-hydraulic calcium silicates cements: mechanism, carbonation and performance. Cem Concr Compos. 2022;133:104641. doi:10.1016/j.cemconcomp.2022.104641
[15] Moini R. Perspectives in architected infrastructure materials. RILEM Tech Lett. 2023;8:125–140. doi:10.21809/rilemtechlett.2023.183
[16] Ashraf W, Olek J. Carbonation behavior of hydraulic and non-hydraulic calcium silicates: potential of utilizing low-lime calcium silicates in cement-based materials. J Mater Sci. 2016;51:6173–6191. doi:10.1007/s10853-016-9909-4
[17] VANSIL® W Wollastonite-Low Aspect Ratio Grades for Paints & Coatings, Vanderbilt Minerals, LLC; 2018. https://www.vanderbiltminerals.com/resources/TDS_VANSIL_W_Powder_Grades_Web.pdf.
[18] Moini M. Buildability and mechanical performance of architectured cement-based materials fabricated using a direct-ink-writing process. 2020:7489310 Bytes. doi:10.25394/PGS.12413036.V1
[19] Moini M, Olek J, Youngblood JP, et al. Additive manufacturing and performance of architectured cement-based materials. Adv Mater. 2018;30:1802123. doi:10.1002/adma.201802123
[20] Moini R, Olek J, Zavattieri PD, et al. Open-span printing method for assessment of early-age deformations of additively manufactured cement-based materials using an isosceles triangle. In: SZ Jones, EL Kreiger, editor. *Standards development for cement and concrete for Use in additive construction, 100 Barr Harbor Drive, PO Box C700, West Conshohocken, PA 19428-2959*; 2021. p. 1–12. doi:10.1520/STP163620200089
[21] Lyu F, Zhao D, Hou X, et al. Overview of the development of 3D-printing concrete. A review. Appl Sci. 2021;11:9822. doi:10.3390/app11219822
[22] Chen Y, He S, Gan Y, et al. A review of printing strategies, sustainable cementitious materials and characterization methods in the context of extrusion-based 3D concrete printing. J Build Eng. 2022;45:103599. doi:10.1016/j.jobe.2021.103599
[23] Tay YWD, Ting GHA, Qian Y, et al. Time gap effect on bond strength of 3D-printed concrete. Virtual Phys Prototyp. 2019;14:104–113. doi:10.1080/17452759.2018.1500420
[24] Moini R, Olek J, Zavattieri PD, et al. Early-age buildability-rheological properties relationship in additively manufactured cement paste hollow cylinders. Cem Concr Compos. 2022;131:104538. doi:10.1016/j.cemconcomp.2022.104538
[25] Rodriguez F, Olek J, Moini M, et al. Linking solids content and flow properties of mortars to their three-dimensional printing characteristics. ACI Mater J. 2021;118; doi:10.14359/51733136
[26] Qian Y, Ma S, Kawashima S, et al. Rheological characterization of the viscoelastic solid-like properties of fresh cement pastes with nanoclay addition. Theor Appl Fract Mech. 2019;103:102262. doi:10.1016/j.tafmec.2019.102262
[27] Lu B, Weng Y, Li M, et al. A systematical review of 3D printable cementitious materials. Constr Build Mater. 2019;207:477–490. doi:10.1016/j.conbuildmat.2019.02.144
[28] Marchon D, Kawashima S, Bessaies-Bey H, et al. Hydration and rheology control of concrete for digital fabrication: potential admixtures and cement chemistry. Cem Concr Res. 2018;112:96–110. doi:10.1016/j.cemconres.2018.05.014
[29] Panda B, Unluer C, Tan MJ. Extrusion and rheology characterization of geopolymer nanocomposites used in 3D printing. Compos Part B Eng. 2019;176:107290. doi:10.1016/j.compositesb.2019.107290
[30] Ma S, Qian Y, Kawashima S. Experimental and modeling study on the non-linear structural build-up of fresh cement pastes incorporating viscosity modifying admixtures. Cem Concr Res. 2018;108:1–9. doi:10.1016/j.cemconres.2018.02.022

[31] Kovler K, Roussel N. Properties of fresh and hardened concrete. Cem Concr Res. 2011;41:775–792. doi:10.1016/j.cemconres.2011.03.009
[32] Kazemian A, Yuan X, Cochran E, et al. Cementitious materials for construction-scale 3D printing: laboratory testing of fresh printing mixture. Constr Build Mater. 2017;145:639–647. doi:10.1016/j.conbuildmat.2017.04.015
[33] Ashraf W, Olek J, Tian N. Multiscale characterization of carbonated wollastonite paste and application of homogenization schemes to predict its effective elastic modulus. Cem Concr Compos. 2016;72:284–298. doi:10.1016/j.cemconcomp.2016.05.023
[34] Maddalena R, Hall C, Hamilton A. Effect of silica particle size on the formation of calcium silicate hydrate [C-S-H] using thermal analysis. Thermochim Acta. 2019;672:142–149. doi:10.1016/j.tca.2018.09.003
[35] Moini R, Baghaie A, Rodriguez FB, et al. Quantitative microstructural investigation of 3D-printed and cast cement pastes using micro-computed tomography and image analysis. Cem Concr Res. 2021;147:106493. doi:10.1016/j.cemconres.2021.106493
[36] Moini M, Olek J, Magee B, et al. Additive manufacturing and characterization of architectured cement-based materials via X-ray micro-computed tomography. In: T Wangler, RJ Flatt, editor. *First RILEM Int. Conf. Concr. Digit. Fabr. – Digit. Concr. 2018*. Cham: Springer International Publishing; 2019. p. 176–189. doi:10.1007/978-3-319-99519-9_16
[37] Ghantous RM, Evseeva A, Dickey B, et al. Examining effect of printing directionality on the freezing-and-thawing response of three-dimensional-printed cement paste. Mater J. 2023;120:89–102. doi:10.14359/51738808
[38] Ashraf W, Olek J. Carbonation activated binders from pure calcium silicates: reaction kinetics and performance controlling factors. Cem Concr Compos. 2018;93:85–98. doi:10.1016/j.cemconcomp.2018.07.004
[39] Morandeau A, Thiéry M, Dangla P. Investigation of the carbonation mechanism of CH and C-S-H in terms of kinetics, microstructure changes and moisture properties. Cem Concr Res. 2014;56:153–170. doi:10.1016/j.cemconres.2013.11.015
[40] Kocaba V. Development and evaluation of methods to follow microstructural development of cementitious systems including slags. 2009. doi:10.5075/EPFL-THESIS-4523
[41] Diamond S. Measurement of the viscosity of resins used in SEM specimen preparation. Mater Struct. 2007;40:995–1000. doi:10.1617/s11527-006-9196-7
[42] Walker HN, Lane DS, Stutzman PE. Petrographic methods of examining hardened concrete: a petrographic manual. 1997. doi:10.21949/1404099
[43] Gupta S, Esmaeeli HS, Prihar A, et al. Fracture and transport analysis of heterogeneous 3D-Printed lamellar cementitious materials. Cem Concr Compos. 2023;140:105034. doi:10.1016/j.cemconcomp.2023.105034
[44] Wong HS, Head MK, Buenfeld NR. Pore segmentation of cement-based materials from backscattered electron images. Cem Concr Res. 2006;36:1083–1090. doi:10.1016/j.cemconres.2005.10.006
[45] Abuelma'atti MT. A simple algorithm for fitting measured data to Fourier-series models. Int J Math Educ Sci Technol. 1993;24:107–112. doi:10.1080/0020739930240114
[46] Panwar P, Gopal G, Kumar R. Image Segmentation using K-means clustering and thresholding. Image (IN). 2016;3:1787–1793.
[47] Akhnoukh AK, Buckhalter C. Ultra-high-performance concrete: constituents, mechanical properties, applications and current challenges. Case Stud Constr Mater. 2021;15:e00559. doi:10.1016/j.cscm.2021.e00559
[48] Ashraf W, Olek J, Sahu S. Phase evolution and strength development during carbonation of low-lime calcium silicate cement (CSC). Constr Build Mater. 2019;210:473–482. doi:10.1016/j.conbuildmat.2019.03.038
[49] Liu J, Ren F, Quan H. Prediction model for compressive strength of porous concrete with low-grade recycled aggregate. Materials (Basel). 2021;14:3871. doi:10.3390/ma14143871
[50] Chang C-F, Chen J-W. The experimental investigation of concrete carbonation depth. Cem Concr Res. 2006;36:1760–1767. doi:10.1016/j.cemconres.2004.07.025
[51] Sun J, Bertos MF, Simons SJR. Kinetic study of accelerated carbonation of municipal solid waste incinerator air pollution control residues for sequestration of flue gas CO2. Energy Environ Sci. 2008;1:370. doi:10.1039/b804165 m
[52] Lo Y, Lee HM. Curing effects on carbonation of concrete using a phenolphthalein indicator and fourier-transform infrared spectroscopy. Build Environ. 2002;37:507–514. doi:10.1016/S0360-1323(01)00052-X
[53] Behnia B, Aali Anvari A, Safardoust-Hojaghan H, et al. Positive effects of novel nano-zirconia on flexural and compressive strength of Portland cement paste. Polyhedron. 2020;177:114317. doi:10.1016/j.poly.2019.114317
[54] Liu J, Fu J, Yang Y, et al. Study on dispersion, mechanical and microstructure properties of cement paste incorporating graphene sheets. Constr Build Mater. 2019;199:1–11. doi:10.1016/j.conbuildmat.2018.12.006
[55] Mousavi MA, Bahari A. Influence of functionalized MWCNT on microstructure and mechanical properties of cement paste. Sādhanā. 2019;44:103. doi:10.1007/s12046-019-1087-z
[56] Peng Y, Unluer C. Development of alternative cementitious binders for 3D printing applications: a critical review of progress, advantages and challenges. Compos Part B Eng. 2023;252:110492. doi:10.1016/j.compositesb.2022.110492
[57] Jafari D, van Alphen KJH, Geurts BJ, et al. Porous materials additively manufactured at low energy: single-layer manufacturing and characterization. Mater Des. 2020;191:108654. doi:10.1016/j.matdes.2020.108654